Mn-Doped Quinary Ag–In–Ga–Zn–S Quantum Dots for Dual-Modal Imaging

Perizat Galiyeva, Hervé Rinnert, Sabine Bouguet-Bonnet, Sebastien Leclerc, Balan Lavinia, Halima Alem, Sébastien Blanchard, Jordane Jasniewski, Ghouti Medjahdi, Bolat Uralbekov, et al.

▶ **To cite this version:**

Perizat Galiyeva, Hervé Rinnert, Sabine Bouguet-Bonnet, Sebastien Leclerc, Balan Lavinia, et al.. Mn-Doped Quinary Ag–In–Ga–Zn–S Quantum Dots for Dual-Modal Imaging. ACS Omega, 2021, 6 (48), pp.33100 - 33110. 10.1021/acsomega.1c05441 . hal-03469094

HAL Id: hal-03469094
https://hal.univ-lorraine.fr/hal-03469094v1

Submitted on 7 Dec 2021

HAL is a multi-disciplinary open access archive for the deposit and dissemination of scientific research documents, whether they are published or not. The documents may come from teaching and research institutions in France or abroad, or from public or private research centers.

L'archive ouverte pluridisciplinaire **HAL**, est destinée au dépôt et à la diffusion de documents scientifiques de niveau recherche, publiés ou non, émanant des établissements d'enseignement et de recherche français ou étrangers, des laboratoires publics ou privés.

Distributed under a Creative Commons Attribution 4.0 International License

ACS OMEGA

http://pubs.acs.org/journal/acsodf

Article

Mn-Doped Quinary Ag−In−Ga−Zn−S Quantum Dots for Dual-Modal Imaging

Perizat Galiyeva, Hervé Rinnert, Sabine Bouguet-Bonnet, Sébastien Leclerc, Lavinia Balan, Halima Alem, Sébastien Blanchard, Jordane Jasniewski, Ghouti Medjahdi, Bolat Uralbekov, and Raphaël Schneider*

Cite This: *ACS Omega* 2021, 6, 33100−33110

Read Online

ACCESS | Metrics & More | Article Recommendations | Supporting Information

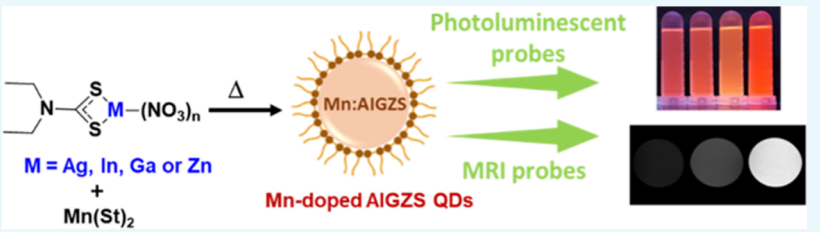

ABSTRACT: Doping of transition metals within a semiconductor quantum dot (QD) has a high impact on the optical and magnetic properties of the QD. In this study, we report the synthesis of Mn^{2+}-doped Ag−In−Ga−Zn−S (Mn:AIGZS) QDs via thermolysis of a dithiocarbamate complex of Ag^{+}, In^{3+}, Ga^{3+}, and Zn^{2+} and of $Mn(stearate)_2$ in oleylamine. The influence of the Mn^{2+} loading on the photoluminescence (PL) and magnetic properties of the dots are investigated. Mn:AIGZS QDs exhibit a diameter of ca. 2 nm, a high PL quantum yield (up to 41.3% for a 2.5% doping in Mn^{2+}), and robust photo- and colloidal stabilities. The optical properties of Mn:AIGZS QDs are preserved upon transfer into water using the glutathione tetramethylammonium ligand. At the same time, Mn:AIGZS QDs exhibit high relaxivity (r_1 = 0.15 mM^{-1} s^{-1} and r_2 = 0.57 mM^{-1} s^{-1} at 298 K and 2.34 T), which shows their potential applicability for bimodal PL/magnetic resonance imaging (MRI) probes.

1. INTRODUCTION

Single-modal imaging techniques such as photoluminescence (PL) imaging and magnetic resonance imaging (MRI) are widely used as diagnostic tools and for the monitoring of biological processes in living organisms. However, each imaging modality has its inherent advantages and limitations. PL imaging is relatively easy to use and exhibits a high sensitivity but its resolution is weak to get three-dimensional (3D) anatomical information.[1,2] On the contrary, MRI suffers from its low sensitivity but allows the 3D imaging of opaque and soft tissues with high spatial resolution and deep tissue penetration.[3,4] Thus, the development of bimodal probes combining sensitivity and spatial resolution is of high interest for whole body imaging.

In recent years, the development of nanoparticles with both PL and MR functionalities has been the object of tremendous efforts.[5−8] For more than 20 years, semiconductor quantum dots (QDs) have received high attention as optical contrast agents. Compared to conventional organic fluorophores, QDs exhibit unique optical properties including broad absorption bands, size- and composition-tunable PL emission, and high brightness and photostability.[9−11] Numerous strategies like the assembly of QDs with paramagnetic Fe_3O_4 nanoparticles,[12−14] the deposition of a paramagnetic coating at the surface of QDs, or the reverse option consisting in the deposition of QDs at the surface of Fe_3O_4 nanoparticles,[15−17] or finally, the conjugation of QDs with Gd^{3+} chelates[18−20] have been developed to prepare probes for bimodal imaging. However, some of these nanoparticles have shortcomings such as the decrease of the PL intensity after association with the magnetic center, a high hydrodynamic diameter, or tedious synthesis methods. Another strategy is the doping of QDs with paramagnetic cations, usually, Gd^{3+},[21,22] but the use of Fe^{3+} has also been reported.[23] Although Gd^{3+} complexes are usually considered safe for clinical applications,[24] Gd^{3+} may exhibit toxicity and its administration may conduct to the development of nephrogenic systemic fibrosis for patients suffering from severe renal impairment.[25] Mn^{2+} has lower toxicity, exhibits a relaxivity similar to that of Gd^{3+} and has been demonstrated to be a valuable alternative as a dopant to Gd^{3+} for engineering nanocrystals for bimodal imaging. Binary CdS,[26] PbS,[27] ZnS,[28,29] and ZnSe,[30−32] ternary In−Zn−S,[33] and quaternary Cu−In−Zn−S (CIZS) and Cu−In−Zn−Se (CIZSe) QDs[34−36] have successfully been doped with Mn^{2+} ions for combined PL and MR imaging.

Received: September 30, 2021
Accepted: November 15, 2021
Published: November 23, 2021

Downloaded via 193.54.42.94 on December 7, 2021 at 13:06:06 (UTC).
See https://pubs.acs.org/sharingguidelines for options on how to legitimately share published articles.

© 2021 The Authors. Published by American Chemical Society

Scheme 1. Schematic Representation of Mn-Doped AIGZS QD Synthesis

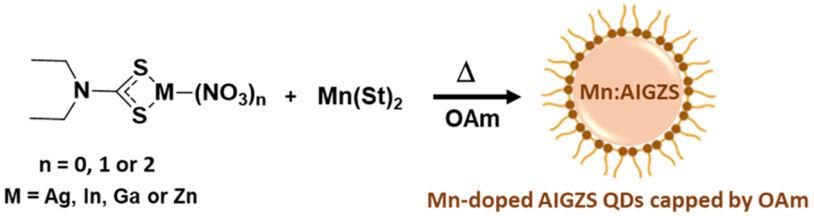

We recently reported the synthesis of highly luminescent quinary Ag−In−Ga−Zn−S (AIGZS) QDs via thermal decomposition in oleylamine (OAm) of a single $Ag_xIn_yGa_{2-x-y}Zn_2(S_2CN(C_2H_5)_2)_4$ dithiocarbamate precursor.[37] In this study, we used the heavy-metal-free AIGZS QDs as host nanocrystals to incorporate Mn^{2+} dopants, and the dual functional (PL/MRI) properties of the doped QDs were investigated. Our results showed that Mn-doped AIGZS (Mn:AIGZS) QDs exhibited the Mn^{2+}-related $^4T_1 \rightarrow {}^6A_1$ PL with a PL quantum yield (PL QY) of up to 41.3% and a high PL lifetime of up to 887.9 μs. The dependence of the PL QY and the PL lifetime of Mn:AIGZS QDs on the Mn^{2+} loading was demonstrated. Mn:AIGZS QDs could easily be transferred into aqueous solution using the hydrophilic glutathione tetramethylammonium (GTMA) ligand without alteration of their optical properties and were demonstrated to show high relaxivity (r_1 = 0.15 mM^{-1} s^{-1} and r_2 = 0.57 mM^{-1} s^{-1} at 2.34 T). Due to their long PL lifetime that allows to improve the temporal discrimination of the PL signal from the autofluorescence background, to their photostability and to their high relaxivity, Mn:AIGZS QDs should have attractive applications in bioimaging.

2. RESULTS AND DISCUSSION

2.1. Synthesis of Mn-Doped AIGZS QDs and Optical Properties. Mn-doped Ag−In−Ga−Zn−S (Mn:AIGZS) QDs were synthesized in a two-stage process.[37] First, a Ag, In, Ga, and Zn dithiocarbamate complex ($Ag_xIn_yGa_{2-x-y}Zn_2(S_2CN(C_2H_5)_2)_4$) used as a precursor was prepared using a Ag/In/Ga/Zn ratio of 0.25:0.875:0.875:2 to obtain AIGZS QDs that did not emit light in the same spectral window as Mn-doped QDs. The loading in the $MnSt_2$ dopant was calculated relative to the total amount of metal cations and varied from 1 to 10%. Next, the $Ag_xIn_yGa_{2-x-y}Zn_2(S_2CN(C_2H_5)_2)_4$ precursor and $MnSt_2$ were thermally decomposed at 220 °C in OAm used as a solvent and as a capping ligand (Scheme 1). After 10 min of heating for completion of QD growth, the reaction mixture was centrifuged to remove large-sized particles. The surface defects were repaired by reheating Mn:AIGZS QDs of the colloidal solution at 220 °C for 30 min.

In preliminary experiments, we also evaluated a synthetic process involving a dithiocarbamate complex containing Ag^+, In^{3+}, Ga^{3+}, Zn^{2+}, and Mn^{2+} metal cations. As can be seen in Figure S1, similar optical properties were obtained for the Mn(5) and Mn(10):AIGZS QDs using the two synthetic approaches. The loading in Mn^{2+} was found to be much more convenient to control when $Mn(St)_2$ was added to the $Ag_xIn_yGa_{2-x-y}Zn_2(S_2CN(C_2H_5)_2)_4$ precursor, and the synthetic process described in Scheme 1 is kept for further studies.

The accurate compositions of OAm-capped AIGZS and Mn:AIGZS QDs are determined by inductively coupled plasma-optical emission spectrometry (ICP-OES) (Table 1). Using a Ag/In/Ga/Zn precursor ratio of 1:3.5:3.5:8 results in $Ag_1In_{3.07}Ga_{3.33}Zn_{7.40}$ QDs, which indicates that all metal cations are well incorporated in AIGZS QDs. The Ag/In/Ga ratio is weakly affected by the increase of the Mn loading. A slight decrease in the In content and a slight increase in the Ga content are observed when increasing the loading in Mn from 1 to 10%. The influence of the doping on the Zn content is more pronounced. The decrease of the Zn content with the increase of the Mn doping suggests that Mn^{2+} substitutes Zn^{2+} in the AIGZS crystal lattice. Finally, the amount of Mn^{2+} ions loaded in the nanocrystals is lower than the amount used for the synthesis (0.81, 1.96, 4.07, and 5.01% of Mn^{2+} are detected when using 1, 2.5, 5, and 10% of Mn^{2+}, respectively).

Table 1. Compositions of OAm-Capped AIGZS and Mn:AIGZS QDs

Mn loading (%)	experimental composition
0	$Ag_1In_{3.07}Ga_{3.33}Zn_{7.40}$
1	$Ag_1In_{3.06}Ga_{3.33}Zn_{7.37}Mn_{0.12}$
2.5	$Ag_1In_{3.03}Ga_{3.40}Zn_{7.11}Mn_{0.26}$
5	$Ag_1In_{3.03}Ga_{3.44}Zn_{6.81}Mn_{0.55}$
10	$Ag_1In_{2.96}Ga_{3.48}Zn_{6.62}Mn_{0.7}$

Figure 1a shows the UV−vis absorption and the PL emission spectra of AIGZS and Mn-doped AIGZS QDs with loadings in Mn^{2+} of 1, 2.5, 5, and 10%. The absence of distinctive

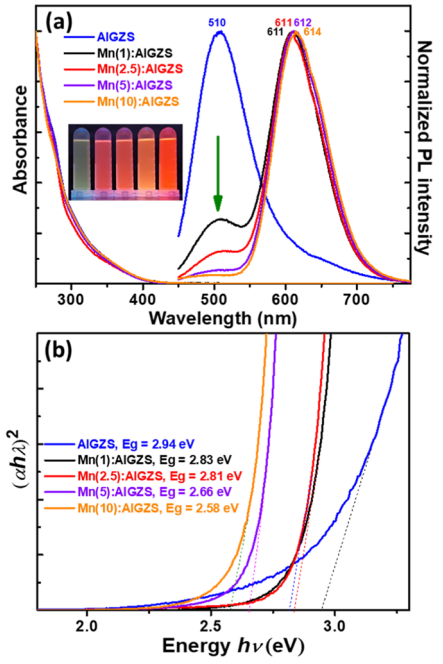

Figure 1. (a) UV−visible and normalized PL emission spectra of AIGZS and Mn:AIGZS QDs (the inset is a digital photograph of the QDs taken under UV light illumination) and (b) determination of optical band gaps of Mn:AIGZS QDs.

https://doi.org/10.1021/acsomega.1c05441
ACS Omega 2021, 6, 33100−33110

absorption is typical for multinary QDs and originates from heterogeneous composition distributions among the dots and thus due to the distribution of vibrational states in AIGZS QDs.[37−39] The absorption spectral profiles of AIGZS and Mn:AIGZS QDs are almost similar, indicating that both the diameter and the composition of the dots are not significantly modified by the doping. The band gap values of the dots are determined from the Tauc plots of $(\alpha h\nu)^2$ vs $h\nu$, where α is the absorption coefficient and $h\nu$ is the photon energy, and are found to decrease from 2.94 for AIGZS QDs to 2.58 eV for Mn(10):AIGZS QDs (Figure 1b). This decrease in the band gap energy with the increase in Mn^{2+} content confirms the substitution of Zn^{2+} ions by Mn^{2+} in the AIGZS crystal lattice previously observed by ICP as the band gap energy of MnS (3.1−3.2 eV) is lower than that of ZnS (3.6 eV). These results also suggest modifications of the electronic states of the AIGZS QDs by the Mn dopant.

Multinary QDs such as CIZS and AIGZS differ from conventional binary QDs as they do not exhibit the excitonic recombination. The relatively broad PL emission with a large Stokes shift originates from surface states (vacancies and dangling bonds) and interstitial states (interstitial atoms and vacancies) that may act as a donor (D) and acceptor (A) for the electron−hole recombination.[37−40] For undoped AIGZS QDs, the D−A PL emission peak is located at 515 nm and a surface defect-related emission centered at ca. 650 nm can also be observed. The PL QY of AIGZS QDs is of 14.3% in toluene. With the introduction and then increase of the Mn^{2+} doping, the D−A emission is gradually quenched and an intense orange-red fluorescence appears at ca. 612 nm regardless of the Mn^{2+} doping percentage (Figure 1a). A marked increase of the PL QY is observed for Mn:AIGZS QDs (37.9, 41.3, 39.1, and 24.9% for the nanocrystals doped with 1, 2.5, 5, and 10% Mn, respectively). The signal at ca. 612 nm can be attributed to Mn *d*-state emission, as demonstrated below, by the analysis of the QD PL lifetime. The full width at half-maximum of the Mn emission is ca. 85 nm, a value consistent with previous reports.[41]

Mn-doped quaternary CIZS and Ag−In−Zn−S (AIZS) QDs have been the subject of several studies in recent years and their optical emission is particularly found to be dependent on the energy band gap, on the position of the valence and conduction bands of the host, and on the radial position of the dopant in the nanocrystals. Usually, the Mn-related emission is attributed to the radiative transition from the low-spin excited state of Mn^{2+} ($^4T_1$) to its high-spin ground state ($^6A_1$). This emission is observed for CIZS or AIZS QDs with an energy band gap larger than that of this Mn^{2+}-related transition energy (dual D−A and Mn emissions can also be observed).[34,36,41−43] On the contrary, only the D−A emission is observed when the host QDs exhibit a band gap smaller than the Mn emission.[35,38,44] These results will be discussed below in the case of AIGZS QDs.

We also investigated the influence of the Mn doping on the PL lifetime of AIGZS QDs. Time-resolved PL emission was recorded at the PL emission maxima of AIGZS and Mn:AIGZS QDs (Figure 1a), and the results are shown in Figure 2 and Table 2. For all of the samples, the PL decay curves are best fitted using a biexponential function $I(t) = A_1 \exp(-t/\tau_1) + A_2 \exp(-t/\tau_2)$, where τ_1 and τ_2 are the time constants of the PL and A_1 and A_2 are the relative weights of the decay components. The average PL lifetimes (τ_{av}) are determined using $\tau_{av} = (A_1\tau_1 + A_2\tau_2)/(A_1 + A_2)$. The PL lifetimes are

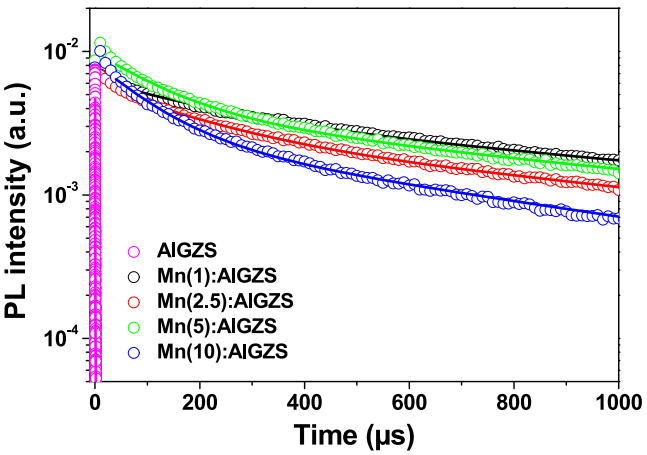

Figure 2. Time-resolved PL spectra of AIGZS and Mn:AIGZS QDs at the PL maximum wavelength.

associated with different electron−hole recombination pathways and can be used to study the PL mechanisms of the dots. Characteristic decay times in the range of 100 ns, here considered as a fast component, and in the range of 100 μs to 1 ms, here considered as a slow component, can be extracted from the experimental curves.

For undoped QDs, the PL decay is characterized by fast components, giving rise to a τ_{av} value close to 100 ns, which can be associated to surface trap-state recombination or to electron−hole recombination from donor−acceptor states (D−A recombination). A marked increase of τ_{av} is observed upon Mn doping (up to 887.9 μs for Mn(1):AIGZS QDs), indicating that the PL emission is not dominated by the D−A recombination but by Mn dopants. The millisecond lifetime measured is indeed related to the $^4T_1 \rightarrow {}^6A_1$ transition of Mn^{2+} ions[45] and further confirms their doping in AIGZS nanocrystals. A decrease of τ_{av} from 887.9 to 293.2 μs is observed when increasing the Mn loading from 1 to 10% likely due to Mn−Mn interactions and/or spin coupling.[44]

The red shift in the PL emission observed compared to conventional binary Mn-doped QDs (ca. 585−590 nm) originates from the complex environment of Mn^{2+} ions in AIGZS QDs and from Mn−Mn coupling that conducts to the splitting between the $^4T_1$ and $^6A_1$ energy levels as previously observed for AIZS and CIZS QDs.[44,46] These Mn−Mn interactions and the defects generated in the AIGZS crystal lattice when increasing the Mn^{2+} loading are also responsible for the decrease of the PL QY and of the PL lifetime of the dots.

Based on the previously described results, possible mechanisms for AIGZS and Mn:AIGZS QDs are depicted in Figure 3. The broad PL emission with a large Stokes shift and the PL lifetime of ca. 100 ns indicate that the PL emission of AIGZS QDs originates from a recombination between intragap donor and acceptor levels, as commonly observed for ternary and quaternary semiconductor nanocrystals (Figure 3a). Due to the relatively wide band gap of AIGZS QDs (2.58 eV), $^4T_1$ and $^6A_1$ Mn states are, respectively, located below and above the donor and acceptor defect states of the AIGZS host (Figure 3b). Upon light excitation, the exciton confined within the donor and acceptor states transfers the energy to the Mn d-states and the Mn-related emission at ca. 612 nm is observed. This emission will not have been observed if we have used the

https://doi.org/10.1021/acsomega.1c05441
ACS Omega 2021, 6, 33100−33110

Table 2. PL QYs, τ_1 and τ_2 Time Constants, and the Contributions of Decays A_1 and A_2 of Undoped and Mn:AIGZS QDs

sample	PL QYs (%)	A_1	τ_1 (μs)	A_2	τ_2 (μs)	τ_{av} (μs)
AIGZS	14.3	0.829	66.3×10^{-3}	0.171	262.3×10^{-3}	99.9×10^{-3}
Mn(1):AIGZS	37.9	0.482	232.5	0.518	1497.4	887.9
Mn(2.5):AIGZS	41.3	0.577	192.4	0.423	1212.3	624.3
Mn(5):AIGZS	39.1	0.643	127.5	0.357	946.3	419.9
Mn(10):AIGZS	24.9	0.702	105.7	0.298	734.5	293.2

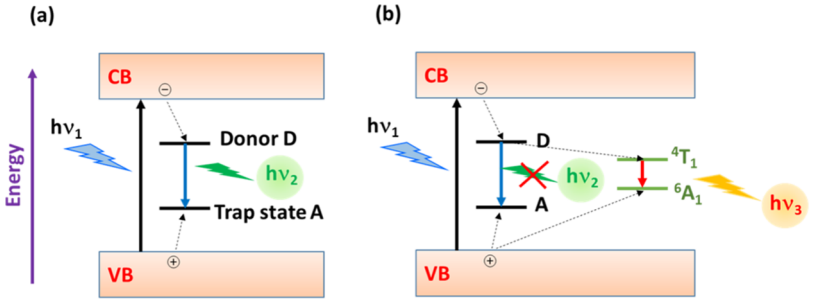

Figure 3. Schematic representation of the PL emission mechanism for (a) AIGZS and (b) Mn:AIGZS QDs.

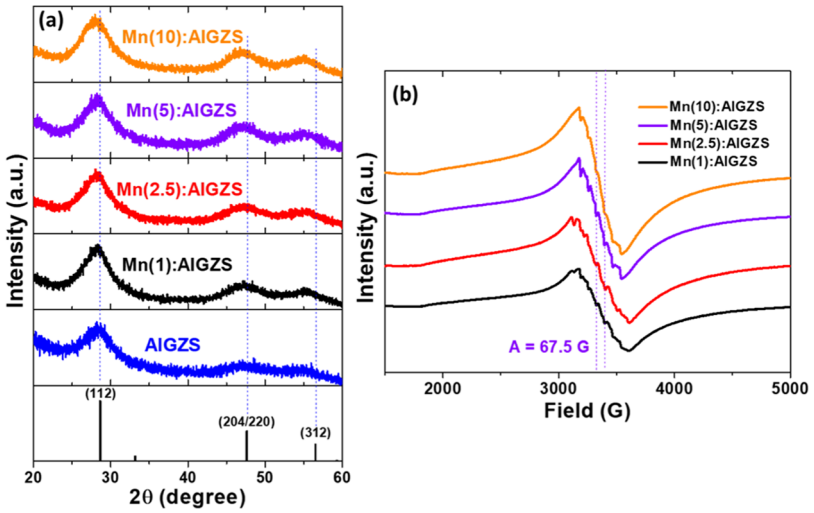

Figure 4. (a) XRD patterns of AIGZS and Mn:AIGZS QDs and (b) electron paramagnetic resonance (EPR) spectra of Mn:AIGZS QDs.

AIGZS host with a lower band gap as described in our previous report.[38]

2.2. Structure and Morphology. X-ray diffraction (XRD) patterns of OAm-capped AIGZS and Mn:AIGZS QDs are shown in Figure 4a. The broad diffraction peaks can be attributed to the nanocrystalline size of the dots. The peaks located at 28.63, 47.63, and 56.52° correspond to the (112), (204/220), and (312) planes of the tetragonal chalcopyrite phase, respectively, and no extra peak or impurities can be detected. The average diameter of AIGZS and Mn:AIGZS QDs was determined to be ca. 2.0 nm based on the Debye–Scherrer equation using the (112) diffraction peak. As can be seen from the figure, the peaks are shifted toward lower angles when the doping in Mn increases. Based on ICP-OES results, this likely originates from the diffusion of Mn^{2+} ions into the QD core, which leads to a lattice expansion since the ionic radius of Mn^{2+} (0.066 nm) is higher than that of Zn^{2+} (0.06 nm).

Electron paramagnetic resonance (EPR) spectra of Mn:AIGZS QDs further confirm the doping of Mn^{2+} ions into the AIGZS nanocrystals (Figure 4b). Though detectable, the six hyperfine splitting related to the coupling of the electronic spin with the 5/2 nuclear spin of Mn^{2+} are ill resolved, probably due to a broadening of the signal originating either from Mn–Mn dipolar interactions[47] and/or to the complex environment of Mn^{2+} surrounded by Ag^{+}, Ga^{3+}, In^{3+}, and Zn^{2+} ions.[41] Indeed, it has been proposed that structural defects in multinary QDs such as AIGZS generate random perturbations to the Mn^{2+} electron–nuclear hyperfine coupling.[34] However, an estimation of the hyperfine constant A of 67.5 G can still be extracted from the partially resolved 6-line pattern, suggesting that at least part of the Mn^{2+} cations are doped into the AIGZS tetragonal lattice and not located at their surface.[41,48]

Mn:AIGZS QDs were further characterized by transmission electron microscopy (TEM). Figure 5a shows a representative TEM of Mn(2.5):AIGZS QDs, indicating that the nanocrystals are nearly spherical in shape with a fairly monodisperse size distribution (1.9 ± 0.5 nm by analyzing ca 100 nanocrystals in the TEM image). Similar results are observed for all Mn-doped AIGZS QDs, indicating that the average diameter of the dots is independent of the Mn^{2+} loading. The high crystallinity of the

https://doi.org/10.1021/acsomega.1c05441
ACS Omega 2021, 6, 33100−33110

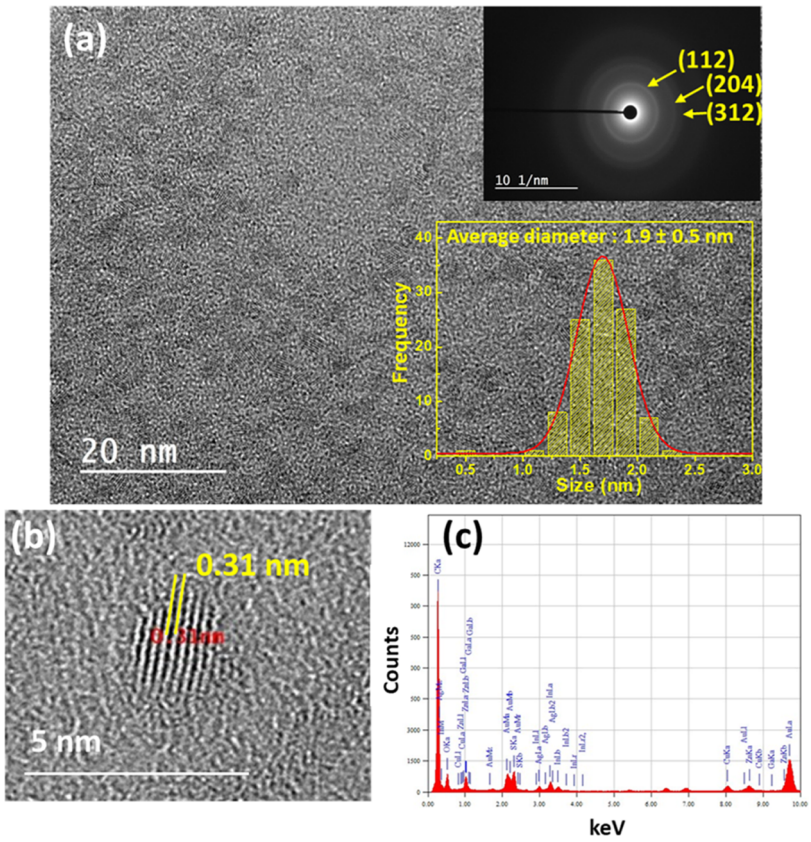

Figure 5. (a) TEM image of Mn(2.5):AIGZS QDs (the insets are the size distribution and the SAED pattern), (b) high-resolution TEM (HRTEM) image of Mn(2.5):AIGZS QDs, and (c) EDX spectrum of the nanocrystals.

dots is confirmed from the selected area electron diffraction (SAED) patterns (inset of Figure 5a). A few larger particles composed of 2−3 nanocrystals and with sizes around 7−9 nm could also be observed on the TEM image. The lattice spacing measured is of ca. 0.31 nm and corresponds to the (112) diffraction plane of the tetragonal chalcopyrite phase (Figure 5b). Finally, the elemental composition of the sample is analyzed by energy-dispersive X-ray spectroscopy (EDX), which shows the presence of Ag, In, Ga, Mn, and S elements and further confirms that Mn^{2+} is successfully doped into AIGZS QDs (Figure 5c).

The presence of Ag, In, Ga, Zn, Mn, and S elements is further confirmed by X-ray photoelectron spectroscopy (XPS) (see Figure S2 for the overview spectrum). The peaks at 367.67, 445.75, 452.28, 1118.26, 1021.79, and around 641.2 eV can be assigned to Ag $3d_{5/2}$, In $3d_{5/2}$, In $3d_{3/2}$, Ga $2p_{3/2}$, Zn $2p_{3/2}$, and Mn $2p_{3/2}$, respectively, and confirm that the elements are in their expected valence states (Ag^{+}, In^{3+}, Ga^{3+}, Zn^{2+}, Mn^{2+}, and S^{2-}) (Figure S3). The Mn $3p_{3/2}$ signal appears at 641.2 eV, which is consistent with values reported for Mn^{2+} doped into ternary or quaternary nanocrystals.[49]

2.3. Magnetic Properties. In the first set of experiments, magnetic measurements using vibrating sample magnetometry (VSM) were carried out for undoped and Mn:AIGZS QDs at 10 and 310 K (Figure 6a,b). As expected, undoped AIGZS QDs exhibit a diamagnetic behavior (blue curve). For Mn-doped QDs, the magnetization curves show that the samples exhibit superparamagnetic behavior as evidenced by values of coercivity and remanence close to zero, thus confirming the onset of the superparamagnetic regime at 10 K (Figure 6a). In contrast, the samples display a clear paramagnetic behavior at 310 K (Figure 6b). The relatively low Ms values (i.e the maximum value is 1.13 emu/g for the 10% doped sample at 310 K) are not surprising owing to the low amount of incorporated Mn compared to the other element. The increase of the magnetization with the Mn loading is nevertheless witnessed at both temperatures (Figure 6a,b). Besides, the influence of the temperature is clearly demonstrated as the magnetic properties are enhanced by decreasing the temperature regardless of the loading amount of Mn (see Figure 6c for Mn(10):AIGZS QDs and Figure S4 for the other doped nanocrystals). These results confirm the efficiency of the Mn doping to produce QDs combining fluorescence and superparamagnetic behavior.

2.4. Aqueous Phase Transfer. Mn:AIGZS QDs were transferred into an aqueous phase using glutathione tetramethylammonium (GTMA) that displaces the native hydrophobic OAm ligand and bounds to the surface of the dots via metal−S bonds (Figure 7a).[50] The resultant dispersion of AIGZS QDs is transparent, indicating that the nanocrystals are well dispersed in aqueous solution (Figure 7b). AIGZS@GTMA QDs can be stored for months in water without alteration of their optical properties, which indicates high colloidal stability.

A representative TEM image of Mn(2.5):AIGZS@GTMA QDs shows that the nanocrystals remain well-dispersed after the ligand exchange and that their average diameter is similar to that of native OAm-capped QDs (2.0 ± 0.6 nm) (Figure 8a). Their tetragonal crystalline structure also remains unaffected as can be seen in Figure 8b. The UV−visible and the PL emission spectra of Mn(2.5):AIGZS QDs selected as a representative indicate that the optical properties of

https://doi.org/10.1021/acsomega.1c05441
ACS Omega 2021, 6, 33100−33110

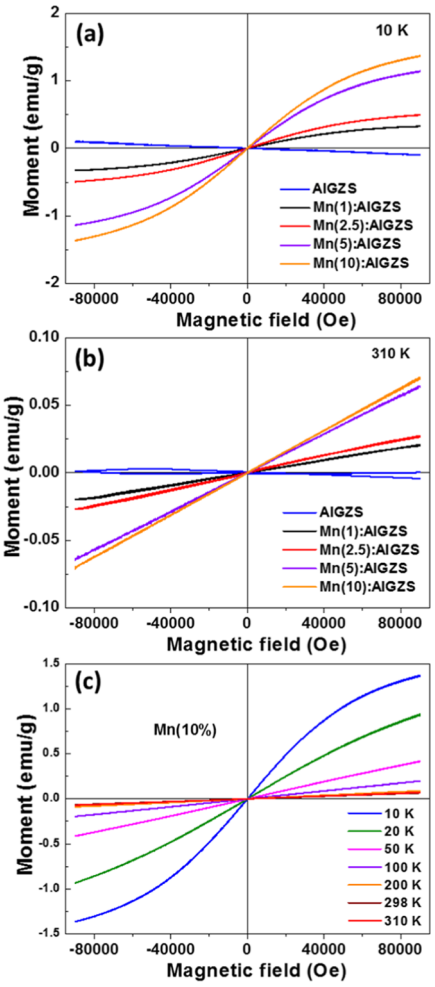

Figure 6. M(H) loop curves of Mn:AIGZS QDs at (a) 10 K and (b) 310 K and (c) M(H) loop curves of Mn(10):AIGZS QDs at different temperatures.

Mn(2.5):AIGZS QDs are well preserved after transferring to water (Figure 8c). Upon ligand exchange, no shift of PL emission wavelength could be detected but a slight drop of PL QYs was observed (35.3, 38.4, 36.8, and 21.7% for AIGZS doped with 1, 2.5, 5, and 10% Mn, respectively).

The ζ-potential of Mn(2.5):AIGZS QDs is -58.5 ± 1.2 mV due to the negatively charged carboxylate functions of the GTMA ligand (Figure 9a). Their hydrodynamic diameter is of 13.7 ± 1.9 nm with a polydispersity index (PDI) of ca. 0.11, further confirming that the QDs are well dispersed in aqueous solution (Figure 9b). AIGZS@GTMA QDs were also found to be stable between pH 4 and 12 (Figure 9c). No significant shift of the PL emission wavelength is observed in this pH range but a marked decrease of the PL intensity occurs below pH 4 due to the protonation of the carboxylate functions, leading to the aggregation of the dots. A similar decrease is observed above pH 12 due to the decomposition of the QD surface into metal hydroxides. The dangling bonds formed act as traps for photogenerated electrons and quench the PL.[51] We also investigated the colloidal stability of Mn(2.5):AIGZS QDs by dispersing the dots in NaCl solutions with concentrations varying from 0.2 to 1 M (Figure S5). After 48 h, no aggregation was observed and the dots retained almost the same PL intensity regardless of the ionic strength. Finally, Mn(2.5):AIGZS QDs dispersed in water exhibit high photostability under the continuous irradiation of a Hg−Xe lamp (intensity of 50 mW/cm^2). The PL intensity remained stable during the 60 min of irradiation while that of Rhodamine 6G used as a reference decreased by ca. 45% (Figure 9d). The good colloidal stability associated with the high photostability of Mn:AIGZS QDs demonstrate their potential as photoluminescent probes for real-time monitoring.

2.5. Mn:AIGZS QDs as MRI Probes. Mn:AIGZS QDs were *in vitro* investigated as contrast agents (CAs) for MRI. Surprisingly, similar relaxation rates were obtained for AIGZS QDs doped with 2.5, 5, and 10% Mn. ICP-OES measurements show that the amount of Mn^{2+} ions doped in AIGZS decreases for the QDs doped with 5 and 10% Mn^{2+} (from 4.67 and 5.01% Mn for the native OAm capped to 2.76 and 2.97% after the GTMA ligand exchange, respectively). These results suggest that ca. 2% of the Mn^{2+} ions are present at the surface of AIGZS doped with 5 and 10% Mn^{2+} and that these ions are driven by the OAm ligand during the ligand exchange. The loading in Mn^{2+} only slightly decreased for Mn(1) and Mn(2.5):AIGZS QDs and was found to be 0.77 and 1.86 atom % after the capping exchange.

The performance of GTMA-coated Mn(1) and Mn(2.5):AIGZS QDs as MRI contrast agents was investigated at room temperature on 1.4 and 2.34 T NMR analyzers. The variations of the longitudinal (R_1) and transverse (R_2) relaxation rates vs the molar concentration in Mn are shown in Figure 10a,b. The concentration-independent relaxivities (r_1 and r_2) were determined from the slopes of the concentration-dependent R_1 and R_2, and the values are $r_1 = 0.28$ mM^{-1} s^{-1} and $r_2 = 0.75$ mM^{-1} s^{-1} at 1.4 T and $r_1 = 0.15$ mM^{-1} s^{-1} and $r_2 = 0.57$ mM^{-1} s^{-1} at 2.34 T, respectively.

Figure 7. (a) Schematic representation of the water transfer of AIGZS QDs using the GTMA ligand and (b) digital photograph taken under ambient light of the dots before and after the ligand exchange.

https://doi.org/10.1021/acsomega.1c05441
ACS Omega 2021, 6, 33100−33110

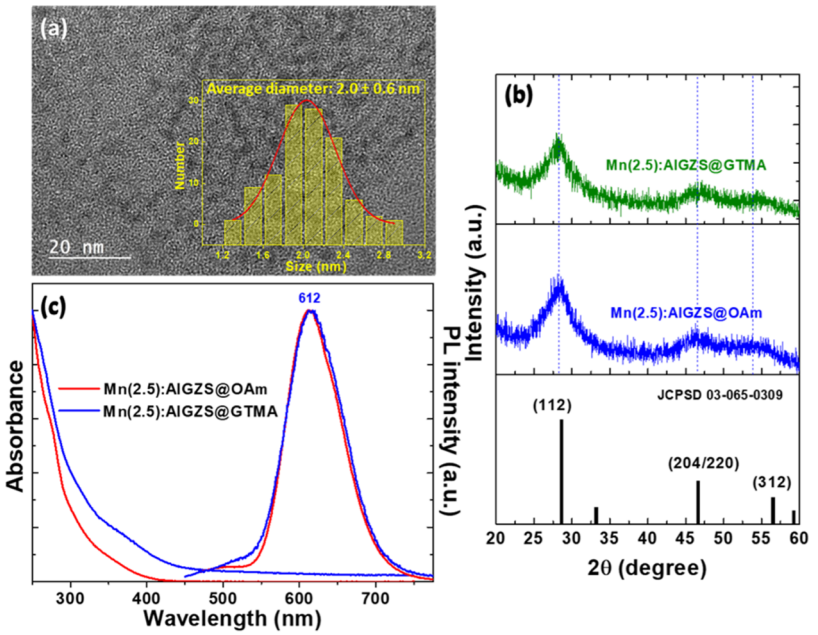

Figure 8. (a) TEM image of Mn(2.5):AIGZS@GTMA QDs (the inset is the size distribution), (b) XRD patterns, (c) UV−visible absorption and PL emission spectra of Mn(2.5):AIGZS QDs before and after the ligand exchange.

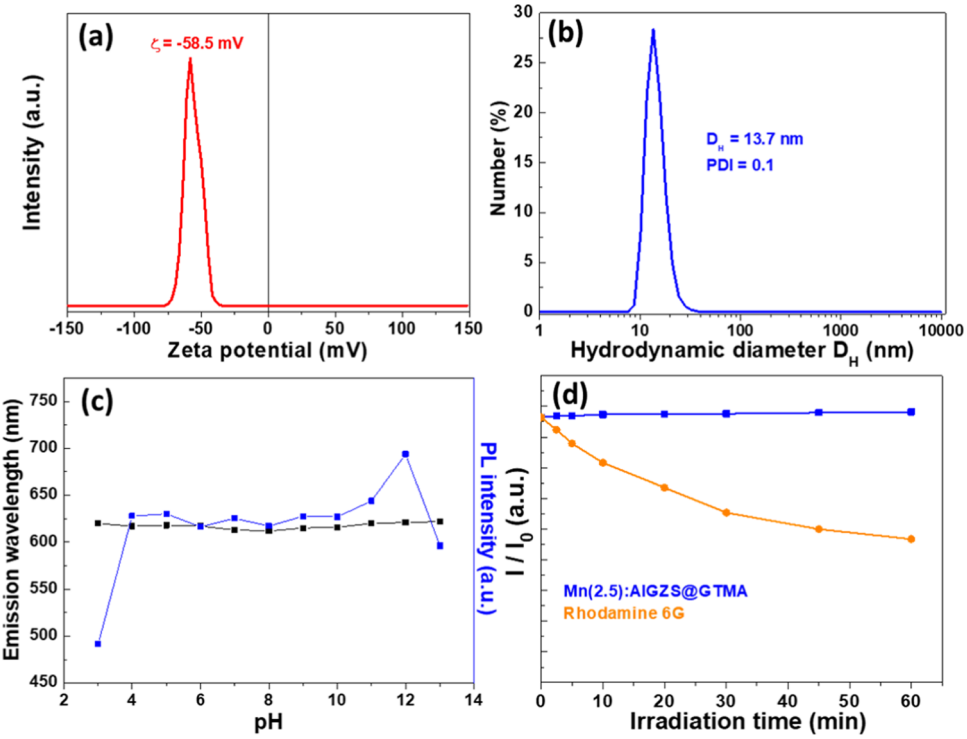

Figure 9. (a) ζ-Potential and (b) hydrodynamic diameter of Mn(2.5):AIGZS@GTMA QDs, (c) evolution of the PL emission wavelength and of the PL intensity with the pH from 3 to 13, and (d) photostability of Mn(2.5):AIGZS QDs and Rhodamine 6G under the continuous irradiation of a Hg−Xe lamp (intensity of 50 mW/cm^2).

To further evaluate the potential of Mn:AIGZS QDs in aqueous solution as contrast agents in MRI, images are recorded at 2.34 T on the same samples (Figure 10c). With the increase of the Mn concentration, the T_1-weighted signal becomes much brighter, while the T_2-weighted one becomes darker, thus confirming that Mn:AIGZS QDs can be used for T_1- and T_2-weighted MRI. Finally, the r_1 values determined for Mn:AIGZS QDs are lower than those of Gd complexes (3.1 mM^{-1} s^{-1}) and of Mn-doped Cu−In−Zn−S QDs.[34,52] This likely originates from the deeper localization of the Mn^{2+} dopant in AIGZS nanocrystals as a doping in the shell is usually used to increase the relaxivity.

3. CONCLUSIONS

In summary, Mn:AIGZS QDs with an average diameter of ca. 2 nm were prepared via a one-pot synthesis involving the thermal

https://doi.org/10.1021/acsomega.1c05441
ACS Omega 2021, 6, 33100−33110

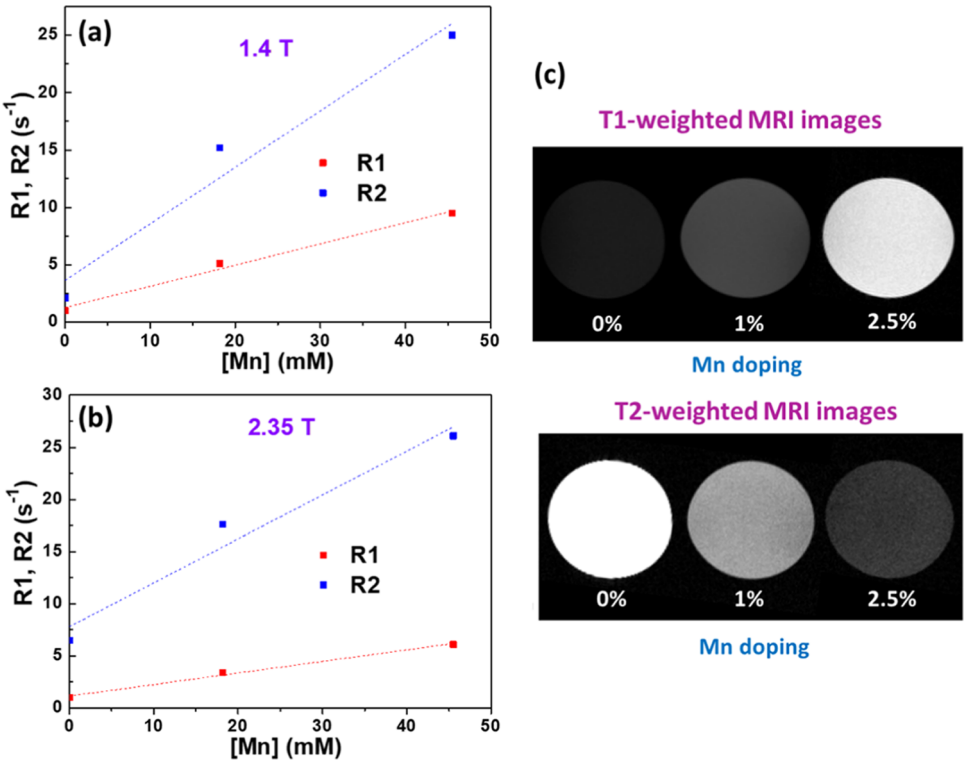

Figure 10. Longitudinal (R_1) and transverse relaxation rates (R_2) of Mn:AIGZS QDs as a function of Mn^{2+} concentration in aqueous solution (a) at 1.4 T, 60 MHz, and 298 K and (b) at 2.34 T, 100 MHz, and 298 K, and (c) T_1-weighted and T_2-weighted images of undoped Mn(1) and Mn(2.5):AIGZS QDs at 2.34 T.

decomposition of $Ag_xIn_yGa_{2-x-y}Zn_2(S_2CN(C_2H_5)_2)_4$ precursors and $Mn(St)_2$ in oleylamine. The obtained QDs show the Mn^{2+} $^4T_1 \rightarrow {}^6A_1$ related PL emission, characterized by high PL QYs (up to 41.3%) and long PL lifetimes (up to 887.9 μs for AIGZS QDs doped with 2.5% Mn). The optical properties were maintained after the oil-soluble Mn:AIGZS QDs were transferred into aqueous solution via ligand exchange, indicating that the dots might be used as photoluminescent probes for bioimaging. Mn:AIGZS QDs can also be used as a contrast agent in MR imaging. Longitudinal relaxivity value (r_1) and transverse relaxivity value (r_2) of 0.15 and 0.57 mM^{-1} s^{-1}, respectively, were determined using a 2.34 T MR imager. These results clearly indicate that Mn:AIGZS QDs have a high potential for dual-modal photoluminescent/MR imaging.

4. EXPERIMENTAL SECTION

4.1. Materials. Silver nitrate $AgNO_3$ (ReagentPlus, >99%, Sigma), gallium nitrate hydrate $Ga(NO_3)_3{\cdot}xH_2O$ (>99.9%, Sigma), indium nitrate hydrate $In(NO_3)_3{\cdot}xH_2O$ (>99.9%, Alfa Aesar), zinc diethyldithiocarbamate $Zn(DDTC)_2$ (97%, Sigma), manganese chloride tetrahydrate $MnCl_2{\cdot}4H_2O$ (99.99%, Sigma), oleylamine (OAm, 80−90%, Acros Organics), stearic acid (>98.5%, Sigma), glutathione (GSH, 99%, Sigma), and tetramethylammonium hydroxide pentahydrate (TMAH, 97%, Sigma) were used as received without any purification.

4.2. Preparation of $Ag_xIn_yGa_{2-x-y}Zn_2(S_2CN(C_2H_5)_2)_4$ Precursors. The single precursor used for the synthesis of AIGZS QDs was prepared according to our previous report.[37] Briefly, $AgNO_3$ (0.25 mmol), $In(NO_3)_3$ (0.875 mmol), $Ga(NO_3)_3$ (0.875 mmol), and $Zn(DDTC)_2$ (2 mmol) (a Ag/In/Ga/Zn molar ratio of 0.25:0.875:0.875:2) were mixed in 10 mL of a 1:1 water−MeOH mixture. The solution was stirred for 2 h at room temperature to form $Ag_xIn_yGa_{2-x-y}Zn_2(S_2CN(C_2H_5)_2)_4$ precursors. The solid obtained was collected by centrifugation (1700g for 15 min), dried under vacuum, and stored at 4 °C until use.

4.3. Synthesis of Mn(+2) Stearate ($MnSt_2$). Under an Ar flow, stearic acid (10 mmol) in 15 mL of MeOH was heated to 50−60 °C until getting a clear solution. After cooling to room temperature, TMAH (10 mmol) dissolved in 20 mL of MeOH was slowly added, and the mixture was stirred for 15 min. Next, $MnCl_2{\cdot}4H_2O$ (5 mmol) dissolved in 10 mL of MeOH was added dropwise, and the mixture was stirred for 2 h at room temperature. The white $MnSt_2$ precipitate was recovered by centrifugation (1700g for 15 min), washed several times with MeOH, dried under vacuum, and stored at 4 °C under N_2 before use.

4.4. Preparation of Mn-Doped Ag−In−Ga−Zn−S (AIGZS) QDs. Mn-doped AIGZS QDs were synthesized by thermolysis of $Ag_xIn_yGa_{2-x-y}Zn_2(S_2CN(C_2H_5)_2)_4$ and $MnSt_2$ using OAm as a solvent. First, the precursor (100 mg) and the appropriate amount of $MnSt_2$ were dispersed in OAm (6 mL) and the mixture was stirred under an Ar flow until getting a clear solution. Then, the mixture was heated at 220 °C and maintained at this temperature for 10 min for completion of nanoparticle growth. After cooling, the large-sized crystals were removed by centrifugation (1700g for 10 min). Mn-doped AIGZS QDs were recovered by precipitation using MeOH followed by centrifugation (2500g for 10 min) and dried under vacuum. Next, the dried QDs were redispersed in OAm (6 mL), and the solution was heated at 220 °C for 30 min. After completion of the reaction, Mn:AIGZS QDs were precipitated by adding an excess of MeOH, recovered by centrifugation

https://doi.org/10.1021/acsomega.1c05441
ACS Omega 2021, 6, 33100−33110

(2500*g* for 10 min), and purified by washing with MeOH. The concentrations of Mn^{2+} ions in AIGZS QDs used through the manuscript are based on the initial concentrations used during the synthesis.

4.5. Transfer of Mn:AIGZS QDs into Water Using Glutathione Tetramethylammonium (GTMA). The ligand exchange with GTMA was conducted using a previously described method.[50] Briefly, GTMA was prepared by reacting GSH (30 mg) and TMAH (54 mg) in 1 mL of MeOH. Separately, 5 mg of the oleophilic Mn:AIGZS@OAm QDs was dispersed in 1 mL of toluene before adding 5 mL of chloroform. Next, 0.5 mL of the GTMA solution was added dropwise to the QD solution and the mixture was vigorously stirred for 2 h at room temperature. Then, water (4.5 mL) was added and the biphasic mixture was slightly shaken to transfer QDs into the aqueous phase before being left for 1 h to reach equilibrium. Finally, the top water layer containing GTMA-capped Mn:AIGZS QDs was collected, precipitated using an excess of MeOH, and centrifuged (2500*g* for 15 min). Mn:AIGZS QDs were stored at 4 °C for further use.

4.6. Morphological, Structural, and Optical Characterizations. The morphology and the microstructure of AIGZS QDs were investigated by transmission electron microscopy (TEM, JEOL-ARM200 Cold FEG microscope operating at 200 keV, equipped with double spherical aberration correctors and fitted with a JEOL SDD CENTURIO EDS system and a Gatan GIF quantum). Selected area electron diffraction (SAED) experiments and EDS analysis were performed on a JEOL ARM 200 Cold FEB transmission electron microscope operating at 200 keV, equipped with double spherical aberration correctors and fitted with a JEOL SD CENTURIO EDS system. The crystal structure of AIGZS QDs was examined by X-ray diffraction (XRD) using a Panalytical X'Pert Pro MPD diffractometer with Cu Kα radiation (λ = 0.15418 nm). X-ray photoelectron spectroscopy (XPS) measurements were carried out with a Gammadata Scienta SES 200-2 spectrometer. Inductively coupled plasma-optical emission spectrometer (ICP-OES) measurements were conducted on a Varian 720-ES equipment. Hydrodynamic QD sizes and ζ-potential measurements were determined by dynamic light scattering (DLS) on a Zetasizer Nano ZS at 25 °C in water (green laser beam 532 nm) with a disposable capillary cell (DTS1070) (Malvern Panalytical, U.K.).

Fourier transform infrared (FTIR) spectra were collected on a Brucker α spectrometer. Optical absorption and PL emission spectra were recorded on a UV−visible absorption spectrometer (Thermo Scientific Evolution 220) and spectrofluorimeter (Horiba Fluoromax-4 Jobin Yvon), respectively. PL spectra were spectrally corrected and PL QYs were determined relative to Rhodamine 6G in ethanol (PL QY = 94%). For the time-resolved photoluminescence (TR-PL) experiments, the QDs were pumped by the 355 nm line of a frequency-tripled YAG (yttrium aluminum garnet):Nd laser. The laser pulse frequency, energy, and duration were typically equal to 10 Hz, 50 μJ, and 10 ns, respectively. The PL signal was analyzed by a monochromator equipped with 600 grooves/mm grating and by a photomultiplier tube cooled at 190 K. The rise time of the detector is equal to around 3 ns.

4.7. Magnetic Measurements. X-band EPR spectra were recorded at 20 K in nonsaturating conditions on a Bruker ELEXSYS 500 spectrometer, equipped with an Oxford instrument continuous-flow liquid-helium cryostat and a temperature control system. Typical conditions were as follows: 5G amplitude modulation, 9.409 GHz, microwave power of 0.63 mW.

Magnetic properties of all synthesized samples were characterized by vibrating sample magnetometry (VSM) with an applied magnetic field (H) of up to ± 9 T. The magnetic moment values are reported in electromagnetic units (emu) per mass unit of the sample.

4.8. Relaxivity Measurements and MR Images. Relaxation rates R_1 and R_2 (inverse of relaxation times T_1 and T_2, respectively) at 60 MHz (^{1}H resonance frequency, corresponding to a magnetic field of 1.4 T) were obtained using a Bruker Minispec MQ60 equipment. Longitudinal (T_1) and transverse (T_2) relaxation times of water protons were measured at 25 °C with the following parameters: T_1 measurements—8 accumulations, repetition time 10 s, inversion recovery with 16 evolution times between 0.001 s and 4 × T_1; T_2 measurements—16 accumulations, repetition time 10 s, Carr−Purcell−Meiboom−Gill experiment with 2000 points, and an interpulse delay of 2 × 0.6 ms.

Relaxation rates at 100 MHz were measured using the same methods and parameters as the ones used at 60 MHz but on a Bruker Biospec Avance 24/40, operating at a magnetic field of 2.34 T (proton resonance frequency of 100 MHz). MR images were acquired on the same spectrometer. The 100 mg/mL solutions of 0, 1, and 2.5% Mn:AIGZS QDs were put in 4 mL vials and imaged with the following parameters: field of view: 6 cm; matrix: 256 × 256 pixels; and slice thickness: 2 mm. Two sets of spin-echo images were acquired: the first one with a 200 ms repetition time and 14 ms echo time to achieve a good T_1 contrast and the T_2-weighted images were recorded with a 5000 ms repetition time and 120 ms echo time.

■ ASSOCIATED CONTENT

Supporting Information

The Supporting Information is available free of charge at https://pubs.acs.org/doi/10.1021/acsomega.1c05441.

UV−visible and PL emission spectra; XPS spectra; and magnetic measurements and colloidal stability (PDF)

■ AUTHOR INFORMATION

Corresponding Author

Raphaël Schneider − *Laboratoire Réactions et Génie des Procédés, Université de Lorraine, 54000 Nancy, France;* orcid.org/0000-0002-6870-6902; Phone: +33 3 72 74 37 90; Email: raphael.schneider@univ-lorraine.fr

Authors

Perizat Galiyeva − *Université de Lorraine, CNRS, LRGP, F-54000 Nancy, France*

Hervé Rinnert − *Université de Lorraine, CNRS, IJL, F-54000 Nancy, France*

Sabine Bouguet-Bonnet − *Université de Lorraine, CNRS, CRM2, F-54000 Nancy, France*

Sébastien Leclerc − *Université de Lorraine, CNRS, LEMTA, F-54000 Nancy, France;* orcid.org/0000-0003-0196-2271

Lavinia Balan − *CEMHTI-UPR 3079 CNRS, Site Haute Température, 45071 Orléans, France;* orcid.org/0000-0003-0144-401X

Halima Alem − *Université de Lorraine, CNRS, IJL, F-54000 Nancy, France;* orcid.org/0000-0002-7918-0504

https://doi.org/10.1021/acsomega.1c05441
ACS Omega 2021, 6, 33100−33110

Sébastien Blanchard − *Sorbonne Université, CNRS, Institut Parisien de Chimie Moléculaire, IPCM, F-75005 Paris, France*
Jordane Jasniewski − *Université de Lorraine, LIBio, F-54000 Nancy, France;* orcid.org/0000-0002-8822-1742
Ghouti Medjahdi − *Université de Lorraine, CNRS, IJL, F-54000 Nancy, France*
Bolat Uralbekov − *Center of Physical-Chemical Methods of Research and Analysis, Al-Farabi Kazakh National University, 050040 Almaty, Kazakhstan; LLP ≪EcoRadSM≫, 050040 Almaty, Kazakhstan*

Complete contact information is available at: https://pubs.acs.org/10.1021/acsomega.1c05441

Author Contributions

Conceptualization, P.G. and R.S.; data curation, P.G., H.R., S.B.-B., S.L., L.B., H.A., S.B., J.J., and G.M.; funding acquisition, B.U. and R.S.; investigation, P.G., H.R., S.B.-B., S.L., L.B., H.A., S.B., J.J., and G.M; project administration, B.U. and R.S.; supervision, H.A., B.U., and R.S.; writing original draft, P.G. and R.S.; and writing the review and editing, all authors contributed. All authors have read and agreed to the published version of the manuscript.

Notes

The authors declare no competing financial interest.

■ ACKNOWLEDGMENTS

The authors thank the Bolashak International Scholarship of JSC "Center for International Programs". This work was supported partly by the French PIA project ≪Lorraine Université d'Excellence≫, reference ANR-15-IDEX-04-LUE, Impact Biomolecules. The authors greatly acknowledge the "Plateforme de RMN de l'Institut Jean Barriol, Université de Lorraine".

■ REFERENCES

(1) Morita, Y.; Sakaguchi, T.; Unno, N.; Shibasaki, Y.; Suzuki, A.; Fukumoto, K.; Inaba, K.; Baba, S.; Takehara, Y.; Suzuki, S.; Konno, H. Detection of hepatocellular carcinomas with near-infrared fluorescence imaging using indocyanine green: its usefulness and limitation. *Int. J. Clin. Oncol.* **2013**, *18*, 232−241.
(2) Vollrath, A.; Schubert, S.; Schubert, U. S. Fluorescence imaging of cancer tissue based on metal-free polymeric nanoparticles—a review. *J. Mater. Chem. B* **2013**, *1*, 1994−2007.
(3) Damadian, R. Tumor detection by nuclear magnetic resonance. *Science* **1971**, *171*, 1151−1153.
(4) Kim, S. G.; Richter, W.; Ugurbil, K. Limitations of temporal resolution in functional MRI. *Magn. Reson. Med.* **1997**, *37*, 631−636.
(5) Jańczewski, D.; Zhang, Y.; Das, G. K.; Yi, D. K.; Padmanabhan, P.; Bhakoo, K. K.; Yang Tan, T. T.; Selvan, S. T. Bimodal magnetic-fluorescent probes for bioimaging. *Microsc. Res. Tech.* **2011**, *74*, 563−576.
(6) Liu, Y.; Ai, K.; Yuan, Q.; Lu, L. Fluorescence-enhanced gadolinium-doped zinc oxide quantum dots for magnetic resonance and fluorescence imaging. *Biomaterials* **2011**, *32*, 1185−1192.
(7) Jing, L.; Ding, K.; Kershaw, S. V.; Kempson, I. M.; Rogach, A. L.; Gao, M. Magnetically Engineered Semiconductor Quantum Dots as Multimodal Imaging Probes. *Adv. Mater.* **2014**, *26*, 6367−6386.
(8) Yong, K.-T. Mn-doped near-infrared quantum dots as multimodal targeted probes for pancreatic cancer imaging. *Nanotechnology* **2009**, *20*, No. 015102.
(9) Michalet, X.; Pinaud, F. F.; Bentolila, L. A.; Tsay, J. M.; Doose, S.; Li, J. J.; Sundaresan, G.; Wu, A. M.; Gambir, S. S.; Weiss, S. Quantum dots for live cells, in vivo imaging, and diagnostics. *Science* **2005**, *307*, 538−544.
(10) Rosenthal, S. J.; Chang, J. C.; Koutun, O.; McBride, J. M.; Tomlinson, I. D. Biocompatible quantum dots for biological applications. *Chem. Biol.* **2011**, *18*, 10−24.
(11) Pandey, S.; Bodas, D. High-quality quantum dots for multiplexed bioimaging: A critical review. *Adv. Colloid Interface Sci.* **2020**, *278*, No. 102137.
(12) Nasrollahi, F.; Sana, B.; Pasamelle, D.; Ahadian, S.; Khademhosseini, A.; Lim, S. Incorporation of Graphene Quantum Dots, Iron, and Doxorubicin in/on Ferritin Nanocages for Bimodal Imaging and Drug Delivery. *Adv. Ther.* **2020**, *3*, No. 1900183.
(13) Chen, Y.; Chen, H.; Zhang, S.; Chen, F.; Zhang, L.; Zhang, J.; Zhu, M.; Wu, H.; Guo, L.; Feng, J.; Shi, J. Multifunctional mesoporous nanoellipsoids for biological bimodal imaging and magnetically targeted delivery of anticancer drugs. *Adv. Funct. Mater.* **2011**, *21*, 270−278.
(14) Yang, F.; Skripka, A.; Tabatabaei, M. S.; Hong, S. H.; Ren, F.; Benayas, A.; Oh, J. K.; Martel, S.; Liu, X.; Vetrome, F.; Ma, D. Multifunctional Self-Assembled Supernanoparticles for Deep-Tissue Bimodal Imaging and Amplified Dual-Mode Heating Treatment. *ACS Nano* **2019**, *13*, 408−420.
(15) Mulder, W. J. M.; Koole, R.; Brandwijk, R. J.; Storm, G.; Chin, P. T. K.; Strijkers, G. J.; de Mello Donega, C.; Nicolay, K.; Griffisen, A. W. Quantum Dots with a Paramagnetic Coating as a Bimodal Molecular Imaging Probe. *Nano Lett.* **2006**, *6*, 1−6.
(16) Labiadh, H.; Ben Chaabane, T.; Sibille, R.; Balan, L.; Schneider, R. A facile method for the preparation of bifunctional Mn:ZnS/ZnS/Fe3O4 magnetic and fluorescent nanocrystals. *Beilstein J. Nanotechnol.* **2015**, *6*, 1743−1751.
(17) Zhang, M.; Wang, W.; Cui, Y.; Chu, X.; Sun, B.; Zhou, N.; Shen, J. Magnetofluorescent Fe_3O_4/carbon quantum dots coated single-walled carbon nanotubes as dual-modal targeted imaging and chemo/photodynamic/photothermal triple-modal therapeutic agents. *Chem. Eng. J* **2018**, *338*, 526−538.
(18) Yang, Y.; Lin, L.; Jing, L.; Yue, X.; Dai, Z. $CuInS_2$/ZnS Quantum Dots Conjugating Gd(III) Chelates for Near-Infrared Fluorescence and Magnetic Resonance Bimodal Imaging. *ACS Appl. Mater. Interfaces* **2017**, *9*, 23450−23457.
(19) Rosenberg, J. T.; Kogot, J. M.; Lovingood, D. D.; Strouse, G. F.; Grant, S. C. Intracellular bimodal nanoparticles based on quantum dots for high-field MRI at 21.1 T. *Magn. Reson. Med.* **2010**, *64*, 871−882.
(20) Pereira, M. I. A.; Pereira, G.; Monteiro, C. A. P.; Geraldes, C. F. G. C.; Cabral Filho, P. E.; Cesar, C. L.; de Thomas, A. A.; Santos, B. S.; Pereira, G. A. L.; Fontes, A. Hydrophilic Quantum Dots Functionalized with Gd(III)-DO3A Monoamide Chelates as Bright and Effective T_1-weighted Bimodal Nanoprobes. *Sci. Rep.* **2019**, *9*, No. 2341.
(21) Yang, W.; Guo, W.; Gong, X.; Zhong, B.; Wang, S.; Chen, N.; Yang, W.; Tu, Y.; Fang, X.; Chang, J. Facile Synthesis of Gd−Cu−In−S/ZnS Bimodal Quantum Dots with Optimized Properties for Tumor Targeted Fluorescence/MR *In Vivo* Imaging. *ACS Appl. Mater. Interfaces* **2015**, *7*, 18759−18768.
(22) Gong, N.; Wang, H.; Li, S.; Deng, Y.; Chen, X.; Ye, L.; Gu, W. Microwave-Assisted Polyol Synthesis of Gadolinium-Doped Green Luminescent Carbon Dots as a Bimodal Nanoprobe. *Langmuir* **2014**, *30*, 10933−10939.
(23) Saha, A. K.; Sharma, P.; Sohn, H. B.; Ghosh, S.; Das, R. K.; Hebard, A. F.; Zeng, H.; Baligand, C.; Walter, G. A.; Moudgil, B. M. Fe doped CdTeS magnetic quantum dots for bioimaging. *J. Mater. Chem. B* **2013**, *1*, 6312−6320.
(24) Rashid, H. U.; Utrera Martines, M. A.; Jorge, J.; de Moraes, P. M.; Umar, M. N.; Khan, K.; Rehman, H. U. Cyclen-based Gd^{3+} complexes as MRI contrast agents: Relaxivity enhancement and ligand design. *Bioorg. Med. Chem.* **2016**, *24*, 5663−5684.
(25) Rogosnitzky, M.; Branch, S. Gadolinium-based contrast agent toxicity: a review of known and proposed mechanisms. *Biometals* **2016**, *29*, 365−376.
(26) Zhao, B.; Huang, P.; Rong, P.; Wang, Y.; Gao, M.; Huang, H.; Sun, K.; Chen, X.; Li, W. Facile synthesis of ternary CdMnS QD-

based hollow nanospheres as fluorescent/magnetic probes for bioimaging. *J. Mater. Chem. B* **2016**, *4*, 1208−1212.
(27) Turyanska, L.; Moro, F.; Patané, A.; Barr, J.; Köchenberger, W.; Taylor, A.; Faas, H. M.; Fowler, M.; Wigmore, P.; Trueman, R. C.; Williams, H.E.L.; Thomas, N. R. Developing Mn-doped lead sulfide quantum dots for MRI labels. *J. Mater. Chem. B* **2016**, *4*, 6797−6802.
(28) Gaceur, M.; Giraud, M.; Hemadi, M.; Nowak, S.; Manguy, N.; Quisefit, J. P.; David, K.; Jahanbin, T.; Benderbous, S.; Boissière, M.; Ammar, S. Polyol-synthesized Zn0.9Mn0.1S nanoparticles as potential luminescent and magnetic bimodal imaging probes: synthesis, characterization, and toxicity study. *J. Nanopart. Res.* **2012**, *14*, No. 932.
(29) Jahanbin, T.; Gaceur, M.; Gros-Dagnac, H.; Benderbous, S.; Merah, S. A. High potential of Mn-doped ZnS nanoparticles with different dopant concentrations as novel MRI contrast agents: synthesis and in vitro relaxivity studies. *J. Nanopart. Res.* **2015**, *17*, No. 258.
(30) Sharma, V. K.; Gokyar, S.; Kelestamur, Y.; Erdem, T.; Unal, E.; Demir, H. V. Manganese Doped Fluorescent Paramagnetic Nanocrystals for Dual-Modal Imaging. *Small* **2014**, *10*, 4961−4966.
(31) Wang, Y.; Wu, B.; Yang, C.; Liu, M.; Sum, T. C.; Yong, K.-T. Synthesis and Characterization of Mn:ZnSe/ZnS/ZnMnS Sandwiched QDs for Multimodal Imaging and Theranostic Applications. *Small* **2016**, *12*, 534−546.
(32) Zhou, R.; Sun, S.; Li, C.; Wu, L.; Hou, X.; Wu, P. Enriching Mn-Doped ZnSe Quantum Dots onto Mesoporous Silica Nanoparticles for Enhanced Fluorescence/Magnetic Resonance Imaging Dual-Modal Bio-Imaging. *ACS Appl. Mater. Interfaces* **2018**, *10*, 34060−34067.
(33) Lai, P.-Y.; Huang, C.-C.; Chou, T.-H.; Ou, K.-L.; Chang, J.-Y. Aqueous synthesis of Ag and Mn co-doped In_2S_3/ZnS quantum dots with tunable emission for dual-modal targeted imaging. *Acta Biomater.* **2017**, *50*, 522−533.
(34) Ding, K.; Jing, L.; Liu, C.; Hou, Y.; Gao, M. Magnetically engineered Cd-free quantum dots as dual-modality probes for fluorescence/magnetic resonance imaging of tumors. *Biomaterials* **2014**, *35*, 1608−1617.
(35) Sitbon, G.; Bouccara, S.; Tasso, M.; François, A.; Bezdetnaya, L.; Marchal, F.; Beaumont, M.; Pons, T. Multimodal Mn-doped I−III−VI quantum dots for near infrared fluorescence and magnetic resonance imaging: from synthesis to *in vivo* application. *Nanoscale* **2014**, *6*, 9264−9272.
(36) Chetty, S. S.; Praneetha, S.; Murugan, A. V.; Govarthanan, K.; Verma, R. S. Human Umbilical Cord Wharton's Jelly-Derived Mesenchymal Stem Cells Labeled with Mn^{2+} and Gd^{3+} Co-Doped $CuInS_2$−ZnS Nanocrystals for Multimodality Imaging in a Tumor Mice Model. *ACS Appl. Mater. Interfaces* **2020**, *12*, 3415−3429.
(37) Galiyeva, P.; Rinnert, H.; Balan, L.; Alem, H.; Medjahdi, G.; Uralbekov, B.; Schneider, R. Single-source precursor synthesis of quinary AgInGaZnS QDs with tunable photoluminescence emission. *Appl. Surf. Sci.* **2021**, *562*, No. 150143.
(38) Galiyeva, P.; Alem, H.; Rinnert, H.; Balan, L.; Blanchard, S.; Medjahdi, G.; Uralbekov, B.; Schneider, R. Highly fluorescent, color tunable and magnetic quaternary Ag−In−Mn−Zn−S quantum dots. *Inorg. Chem. Front.* **2019**, *6*, 1422−1431.
(39) Mrad, M.; Ben Chaabane, T.; Rinnert, H.; Balan, L.; Jasniewski, J.; Medjahdi, G.; Schneider, R. Aqueous Synthesis for Highly Emissive 3 Mercaptopropionic Acid-Capped AIZS Quantum Dots. *Inorg. Chem.* **2020**, *59*, 6220−6231.
(40) Hamanaka, Y.; Ogawa, T.; Tsuzuki, M.; Kuzuya, T. Photoluminescence Properties and Its Origin of $AgInS_2$ Quantum Dots with Chalcopyrite Structure. *J. Phys. Chem. C* **2011**, *115*, 1786−1792.
(41) Manna, G.; Jana, S.; Bose, R.; Pradhan, N. Mn-doped multinary CIZS and AIZS nanocrystals. *J. Phys. Chem. Lett.* **2012**, *3*, 2528−2534.
(42) Peng, L.; Huang, K.; Zhang, Z.; Zhang, Y.; Shi, Z.; Xie, R.; Yang, W. Bandgap- and radial-position-dependent Mn-doped Zn-Cu-In-S/ZnS core/shell nanocrystals. *ChemPhysChem* **2016**, *17*, 752−758.
(43) Sakai, R.; Onishi, H.; Ido, S.; Furumi, S. Effective Mn-doping in $AgInS_2$/ZnS core/shell nanocrystals for dual photoluminescent peaks. *Nanomaterials* **2019**, *9*, No. 263.
(44) Chen, S.; Zaeimian, M. S.; Monteiro, J. H. S. K.; Zhao, J.; Mamalis, A. G.; de Bettencourt-Dias, A.; Zhu, X. Mn doped AIZS/ZnS nanocrystals: Synthesis and optical properties. *J. Alloys Compd.* **2017**, *725*, 1077−1083.
(45) Aboulaich, A.; Geszke, M.; Balan, L.; Ghanbaja, J.; Medjahdi, G.; Schneider, R. Water-based route to colloidal Mn-doped ZnSe and core/shell ZnSe/ZnS quantum dots. *Inorg. Chem.* **2010**, *49*, 10940−10948.
(46) Pradhan, N. Red-Tuned Mn d−d Emission in Doped Semiconductor Nanocrystals. *ChemPhysChem* **2016**, *17*, 1087−1094.
(47) Ishikawa, Y. ESR Spectra of Exchange-Coupled Mn2+ Ions in ZnS and CdS. *J. Phys. Soc. Jpn.* **1966**, *21*, 1473−1481.
(48) Huang, B.; Dai, Q.; Zhuo, N.; Jiang, Q.; Shi, F.; Wang, H.; Zhang, H.; Liao, C.; Cui, Y.; Zhang, J. Bicolor Mn-doped $CuInS_2$/ZnS core/shell nanocrystals for white light-emitting diode with high color rendering index. *J. Appl. Phys.* **2014**, *116*, No. 094303.
(49) Cao, S.; Zhao, J.; Yang, W.; Li, C.; Zheng, J. Mn^{2+}-doped Zn−In−S quantum dots with tunable bandgaps and high photoluminescence properties. *J. Mater. Chem. C* **2015**, *3*, 8844−8851.
(50) Wei, Y.; Yang, J.; Ying, J. Y. Reversible phase transfer of quantum dots and metal nanoparticles. *Chem. Commun.* **2010**, *46*, 3179−3181.
(51) Chetty, S. S.; Praneetha, S.; Murugan, A. V.; Govarthanan, K.; Verma, R. S. Human Umbilical Cord Wharton's Jelly-Derived Mesenchymal Stem Cells Labeled with Mn^{2+} and Gd^{3+} Co-Doped $CuInS_2$−ZnS Nanocrystals for Multimodality Imaging in a Tumor Mice Model. *ACS Appl. Mater. Interfaces* **2020**, *12*, 3415−3429.
(52) Kalavagunta, C.; Michaeli, S.; Metzer, G. J. In vitro Gd-DTPA relaxometry studies in oxygenated venous human blood and aqueous solution at 3 and 7 T. *Contrast Media Mol. Imaging* **2014**, *9*, 169−176.

https://doi.org/10.1021/acsomega.1c05441
ACS Omega 2021, 6, 33100−33110